



**HAL**  
open science

## Indentation response of model oxide dispersion strengthening alloys after ion irradiation up to 700°C

Christian Robertson, Marie-Helene Mathon, B.K. Panigrahi, S. Amirthapandian, S Sojak, Sumita Santra

### ► To cite this version:

Christian Robertson, Marie-Helene Mathon, B.K. Panigrahi, S. Amirthapandian, S Sojak, et al.. Indentation response of model oxide dispersion strengthening alloys after ion irradiation up to 700°C. Journal of Applied Physics, 2022, 132, pp.175107. 10.1063/5.0092138 . cea-03838827

**HAL Id: cea-03838827**

**<https://cea.hal.science/cea-03838827>**

Submitted on 3 Nov 2022

**HAL** is a multi-disciplinary open access archive for the deposit and dissemination of scientific research documents, whether they are published or not. The documents may come from teaching and research institutions in France or abroad, or from public or private research centers.

L'archive ouverte pluridisciplinaire **HAL**, est destinée au dépôt et à la diffusion de documents scientifiques de niveau recherche, publiés ou non, émanant des établissements d'enseignement et de recherche français ou étrangers, des laboratoires publics ou privés.

# Indentation response of model oxide dispersion strengthening alloys after ion irradiation up to 700 °C

Cite as: J. Appl. Phys. **132**, 175107 (2022); <https://doi.org/10.1063/5.0092138>

Submitted: 21 March 2022 • Accepted: 14 October 2022 • Published Online: 03 November 2022

 C. Robertson,  M. H. Mathon, B. K. Panigrahi, et al.



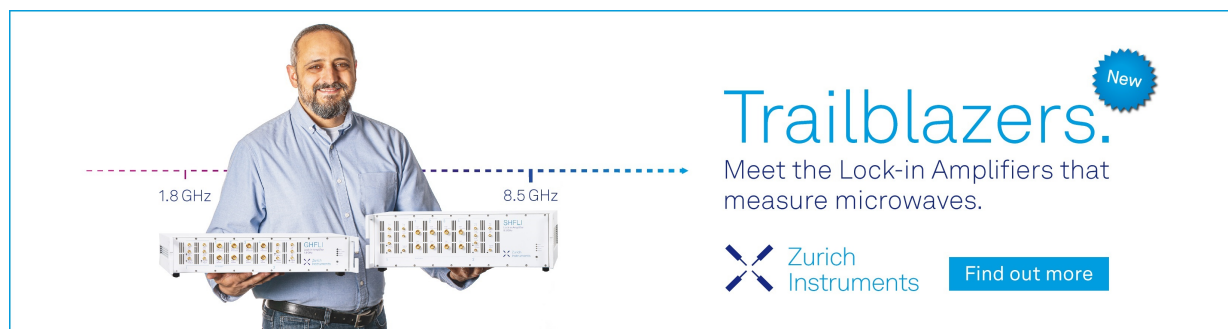
View Online




Export Citation




CrossMark



**Trailblazers.** 

Meet the Lock-in Amplifiers that measure microwaves.

 Zurich Instruments [Find out more](#)

# Indentation response of model oxide dispersion strengthening alloys after ion irradiation up to 700 °C

Cite as: J. Appl. Phys. **132**, 175107 (2022); doi: [10.1063/5.0092138](https://doi.org/10.1063/5.0092138)

Submitted: 21 March 2022 · Accepted: 14 October 2022 ·

Published Online: 3 November 2022



C. Robertson,<sup>1,a)</sup> M. H. Mathon,<sup>1</sup> B. K. Panigrahi,<sup>2</sup> S. Amirthapandian,<sup>2</sup> S. Sojak,<sup>3</sup> and S. Santra<sup>4</sup>

## AFFILIATIONS

<sup>1</sup>CEA, Service de Recherches Métallurgiques Appliquées, Université Paris-Saclay, Gif-sur-Yvette 91191, France

<sup>2</sup>Indira Gandhi Centre for Atomic Research, MSG, Kalpakkam 603 102, Tamil Nadu, India

<sup>3</sup>Faculty of Electrical Engineering and Information Technology, Slovak University of Technology, Ilkovicova 3, 812 19 Bratislava, Slovakia

<sup>4</sup>Characterisation Lab, Quality Assurance, Nuclear Fuel Complex, HBNI, Hyderabad 500 062, India

**Note:** This paper is part of the Special Topic on Radiation Effects in Materials.

**a)** Author to whom correspondence should be addressed: [christian.robertson@cea.fr](mailto:christian.robertson@cea.fr). Tel.: +33 1 69 08 22 70. Fax: +33 1 69 08 71 67

## ABSTRACT

This paper presents an experimental investigation of irradiation-induced evolutions in three different oxide dispersion strengthening (ODS) alloys. High-dose, dual beam Ni-He ion irradiations are carried out up to 700 °C. The significant dose-dependent changes in the ODS particle size and number density are documented and interpreted in terms of specific point defect transport mechanisms, from small angle neutron scattering, TEM, and pulsed low-energy positron system measurements combined. The corresponding micro-mechanical changes in the alloys are evaluated based on the indentation response, which is, in turn, interpreted in terms of related, sub-grain plasticity mechanisms. The room temperature tests (without dwell time) reveal that the microscale work-hardening rate increases with decreasing the particle number density and pronounced strain localization effect. The elevated temperature tests (up to 600 °C, with dwell time) show that the indentation creep compliance is mostly temperature-independent after irradiation up to 25 dpa at  $T_{irr} = 500$  °C and markedly temperature-dependent, after irradiation beyond 40 dpa at  $T_{irr} = 600$  °C. This effect is ascribed to particular creep mechanisms associated with indent-induced plasticity, i.e., high stress and high dislocation density conditions.

Published under an exclusive license by AIP Publishing. <https://doi.org/10.1063/5.0092138>

## I. INTRODUCTION

High-strength materials can be obtained by dispersing nano-sized yttria particles in a metallic matrix.<sup>1,2</sup> Quite naturally, the long-term mechanical properties of these Oxide Dispersion Strengthened (ODS) alloys depend on the stability of the reinforcing particles. The radiation<sup>3–8</sup> and thermal aging<sup>9</sup> effects on particle stability are under investigation by many different groups worldwide. This paper is a contribution of a broader effort carried out at CEA, regarding ODS steel development.<sup>10–18</sup> The particular issue of ODS particle stability in post-irradiated Fe-0.3Y<sub>2</sub>O<sub>3</sub>, Fe-0.2Ti-0.3Y<sub>2</sub>O<sub>3</sub>, and Fe-14Cr-0.2Ti-0.3Y<sub>2</sub>O<sub>3</sub> model alloys (called ODS-1, 2, and 3 for simplicity) has been addressed elsewhere, thanks to TEM and atom probe investigations.<sup>19–21</sup> Complementary SANS

(small angle neutron scattering) and PLEPS (pulsed low-energy positron system) measurements are nonetheless presented in Sec. IV and further interpreted in Sec. V A in support of the distinct, main focus of this paper.

Namely, we attempt linking the dose-dependent microstructural evolutions of model ODS-1, 2, and 3 alloys to corresponding micro-mechanical response and plasticity mechanism changes, using nano-indentation testing at room and elevated temperature, up to 500 °C. In practice, we attempt rationalizing: (1) the post-irradiation indentation response at room temperature, in terms of dislocation-mediated plasticity mechanisms (Sec. V B); (2) the post-irradiation indentation creep response at elevated temperature, in terms of plasticity and point defect transport mechanisms under high stress and high dislocation density conditions (Sec. V C).

This paper is divided into four main sections. The fabrication route of the ODS alloys 1, 2, and 3 is detailed in Sec. II. The experimental techniques employed herein are detailed in Sec. III (Sec. III A: ion irradiation testing conditions, Sec. III B pre- and post-irradiation examinations). The post-irradiation examinations are carried out after high-dose, dual beam Ni–He ion irradiations. Ni and He beams emulate the neutron collision damage and concurrent helium production due to transmutation reactions in nuclear reactors. Sections IV A and IV B presents the observation results performed, respectively, before and after irradiation, in terms of particle size distributions and associated micro-mechanical response. The main radiation-induced changes are analyzed and discussed in Sec. V.

## II. MATERIAL FABRICATION ROUTE

Model alloys ODS-1, 2, and 3 were fabricated using powder metallurgy technique, as described in Refs. 19 and 20 and briefly recalled hereafter. The three selected chemical compositions are

ODS-1: 0.3%Y<sub>2</sub>O<sub>3</sub> and Fe (balance).

ODS-2: 0.2%Ti, 0.3%Y<sub>2</sub>O<sub>3</sub>, and Fe (balance).

ODS-3: 14%Cr, 0.2%Ti, 0.3%Y<sub>2</sub>O<sub>3</sub>, and Fe (balance).

High purity Fe, Ti, Cr, and yttria powders are first milled with the ball to powder ratio (10:1) at 1000 rpm, in the Ar atmosphere at room temperature, during 4 h. These conditions limit the particle size growth and carbon intake, while preserving an adequate mixing of the metal with yttria. Rod-shaped specimens are fabricated by hot extrusion at 1050 °C (ODS-1 and ODS-2), subsequently annealed out at 950 °C during 2 h, and then air cooled. In the ODS-3 case, hot extrusion is carried out at 1150 °C, which is subsequently annealed at 1050 °C during 0.5 h, air cooled, then tempered at 750 °C during 2 h, and, finally, air cooled. The different alloy microstructures and particle distributions were characterized before irradiation as explained in Sec. IV A.

## III. EXPERIMENTAL METHODS

### A. Ion irradiations

The ion irradiation experiments were conducted at JANNUS facilities (Jumelage d'Accélérateurs pour les Nanosciences, le NUcléaire et la Simulation) in Saclay, France. Specimens in the form of 12 mm wide disks (disk thickness = 80 μm) were irradiated using 5 MeV Ni and 1.5 MeV He dual ion beams (beam area = 2 × 2 cm<sup>2</sup>) at  $T_{irr}$  = 500, 600, and 700 °C.

The Ni-related damage and He-implantation profiles are presented in Fig. 1, based on SRIM-2013 (Stopping Range of Ions in Matter software) calculations, using the quick Kinchin–Pease option and a target atom displacement threshold of 40 eV.<sup>22</sup> Information drawn from Fig. 1 includes (i) the Ni-related peak and surface damage levels (see Table I and Sec. IV B 1); (2) the Ni-related damage layer thickness (~2.2 μm), which helps select the (maximum) indenter penetration depth (see Sec. III B); (3) the He-implantation peak depths (0.5 and 1.0 μm), supporting the PLEPS results interpretation (see Sec. IV B 2).

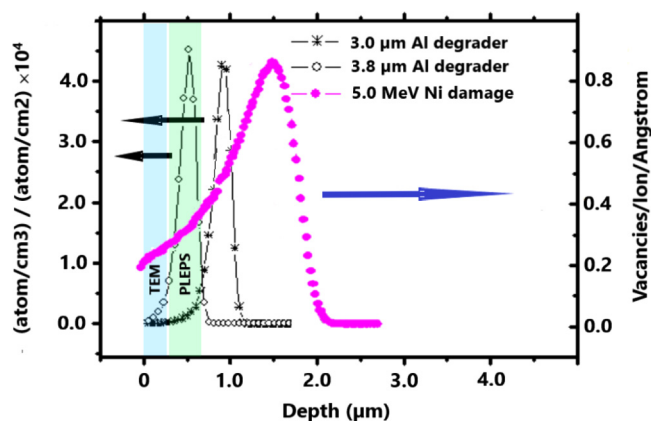


**FIG. 1.** Damage profile due to 5 MeV Ni ion collisions in the Fe–Cr target, along with mitigated 1.5 MeV He co-implantation profiles. The open symbols correspond to implanted He atom profiles [in (atom/cm<sup>3</sup>)/(atom/cm<sup>2</sup>) units] associated with aluminum degrader foil thicknesses 3.0 and 3.8 μm. The implanted He data are indicated in the left-hand vertical axis (arrow marker). The Ni-related damage level (in vacancies/ion/Angström units) is indicated in the right-hand vertical axis (arrow marker). The Ni damage calculation assumes the beam is tilted 15° off-normal, coinciding with the irradiation chamber configuration utilized. He collision damage is neglected, in comparison with the Fe collision damage.

## B. Observation and analysis methods

### 1. Transmission electron microscopy

A Zeiss TEM operated at 200 kV FEG with a column Omega filter has been used for the present investigations. Chemical analysis is also performed in selected TEM foil portions, using electron energy loss spectroscopy (EELS). The TEM foils were cut parallel to the ion irradiated surfaces using the backside electro-polishing technique, where the (ion) beam facing surface is protected by a deposited polymer film, which is peeled off after the foil cutting operation is completed. This means all the examined TEM foils include the ion-implanted surface itself, thereby avoiding any

**TABLE I.** Dual beam ion irradiations carried out in ODS-1, ODS-2, and ODS-3 specimens. The peak and near-surface damage levels (in dpa units) are estimated using Fig. 1 calculation results (peak and surface values in vacancies/ion/Angström units) times 10<sup>8</sup> Å/cm times the corresponding measured Ni dose (in Ni<sup>2+</sup> 10<sup>16</sup> cm<sup>-2</sup> units), over the target atom density (8.48 × 10<sup>22</sup> atoms/cm<sup>3</sup>). There are no results available for ODS-1 at 700 °C due to beam time and irradiation chamber space limitations.

Irradiation temperature	500 °C	600 °C	700 °C
Specimen fabrication	ODS-1, 2, and 3	ODS-1, 2, and 3	ODS-2, ODS-3
He dose (10 <sup>16</sup> He <sup>+</sup> cm <sup>-2</sup> )	2.6	2.7	5.9
Ni dose (10 <sup>16</sup> Ni <sup>2+</sup> cm <sup>-2</sup> )	7.8	7.9	15.2
Peak damage (dpa)	75	75	150
Near-surface damage (dpa)	25	25	40

microstructural changes due to the injected atom concentrations, at the Ni implantation peak (situated beyond  $1.6\ \mu\text{m}$  depth: not shown in Fig. 1). The depth region assessed by TEM is comprised between 0 and 150–200 nm, depending on the foil region examined.

## 2. Small angle neutron scattering

TEM information on particle size distribution and particle density is cross-checked by comparison with Small Angle Neutron Scattering (SANS) analysis. SANS experiments were performed at the Laboratoire Léon Brillouin (CEA-CNRS), Saclay, France, using the «PAXE» small-angle spectrometer device. The specimens used for SANS measurements are cut in the form of  $0.3\ \text{mm}$  thick,  $3\ \text{mm}$  diameter disks. Wavelengths, sample-to-detector distances, and scattering vector ( $q$ ) range used are specified elsewhere.<sup>23,24</sup> The measurements are performed at room temperature under a saturating magnetic field perpendicular to the incident neutron beam direction. The applied magnetic field separates the specimen magnetic and nuclear scattering cross sections and produces specific «A» ratio conditions. The analysis is carried out in two steps using exactly the same assumptions and methods as explained in Ref. 23. Theoretical ratios ( $A_{\text{th}}$ ) are computed first, assuming various well-defined particle chemical compositions and size distributions. These values are then compared with measured ones, which allow evaluating each specimen configuration.

## 3. Nano-indentation at room and elevated temperature, with and without dwell time

The specimen micro-mechanical response is evaluated using nano-indentation technique, equipped with a high-temperature test module (Micro-Materials TM). The as-cut specimen surfaces were mirror-polished using grit papers down to grade 1200 and then, using  $1\ \mu\text{m}$  diamond paste. These surfaces were further electro-polished at  $-20\ ^\circ\text{C}$  using 10 V applied voltage with a 70% ethanol, 20% ethylene glycol mono-butyl ether, and 10% perchloric acid solution, in order to remove plastic deformation introduced during the mechanical polishing.

The irradiated layer response is influenced by its position on top of a softer un-irradiated substrate.<sup>25</sup> In this configuration, the indenter response depends on indenter penetration depth « $h$ » and on the irradiation hardening to un-irradiated hardness ratio  $H_{\text{irr}}/H_{\text{unirr}}$ .<sup>26,27</sup> In this paper, however, no attempt is made to evaluate the actual  $H_{\text{irr}}$  and  $H_{\text{unirr}}$  quantities as prescribed in Refs. 28–33, for example. Our main goal is to evaluate the radiation-induced changes in terms of quantitative (micro) tensile and creep responses, using alternate analytical methods. The latter allows rationalizing the dose-dependent effects in terms of dislocation-mediated, sub-grain scale plasticity mechanisms (see Secs. V B and V C of this paper and Ref. 34).

Post-irradiation damage concentration varies in the specimen depth direction (see Fig. 1). In this paper, the indentation response is associated with a «representative» damage level, comprised between the surface and peak damage levels (see Table I and «general discussion» below). Two different indenter geometries are being used: «Berkovich» and «cube-corner», each characterized by a specific centerline-to-face angle ( $\theta \approx 65^\circ$  and  $\theta \approx 35^\circ$ ,

respectively). Using indentation data from two different indenter geometries allows us to calculate an equivalent micro-tensile response, based on the analysis method as proposed in Refs. 35 and 36. During the room temperature indentation experiments, a constant load rate of  $1\ \text{mN/s}$  is applied, up to achieving indenter penetration depth  $h = 500\ \text{nm}$ . In practice, the corresponding maximum load varied by no more than 10% from one indentation test to another (20–22 mN, in as-received ODS-1), thanks to the careful surface preparation utilized. The test conditions ensure that the indent-induced plastic zone is practically entirely included (The indent-induced plastic zone extent is up to —four to five times the indenter penetration depth.) within the damage layer thickness itself,<sup>27</sup> thereby minimizing the indentation-size and substrate effects,<sup>25,26</sup> while maximizing the dislocation multiplication contribution to the indentation response, in reference to Sec. V B.

The indentation experiments at elevated temperatures (indentation creep experiments) were carried out at the constant loading rate of  $1\ \text{mN/s}$  up to 20 mN, as the corresponding indenter displacement achieves  $h \approx 500\ \text{nm}$ . Subsequent indenter displacement is then recorded at constant load, up to the selected dwell time (1200 s). A hard and brittle oxide layer usually develops on top of the metallic specimen surface, while testing in air and at elevated temperature ( $>300\ ^\circ\text{C}$ ). This effect can strongly influence the indentation response since our testing device is not equipped with a controlled environment chamber. For this reason, elevated temperature indentation tests are restricted to ODS-3; where the oxide growth is minimal, thanks to its relatively high (14%) chromium content (see Sec. II, above). Further experimental details on indentation testing with dwell time are presented in Sec. IV B 3. The indentation response with dwell time at elevated temperature involves specific, self-climb deformation mechanism, presumably associated with the indent-induced dislocation populations. This fast transport mechanism is consistent with substantial, low-temperature creep compliance, as reported in Refs. 37 and 38. For these and other reasons, indentation data are not directly comparable to conventional testing data (tensile and/or creep tests), as further discussed in Secs. V B and V C.

## 4. Positron annihilation spectroscopy (PLEPS)

PLEPS is a positron lifetime measurement technique, which allows probing material depths comparable to the damage ranges of the present ion irradiations. Namely, the positron energy range is 0.5–18 keV, which probes the 2–550 nm depth range in ferritic ODS alloys.<sup>39</sup> The slow mono-energetic positron beam used here is generated using the NEPOMUC source (NEutron induced POsitrone source MUniCh), from the PLEPS instrument operated by FRM 2 at the Heinz Maier-Leibnitz Zentrum (MLZ), Garching, Germany. The positron beam intensity supplied to the PLEPS system is  $\sim 10^9$  positrons per second. The positron beam diameter at the sample holder is 1 mm.<sup>40</sup> The measurement of positron lifetime is based on the same principles as conventional lifetime techniques, albeit the reference start time is provided by the timer signal.<sup>41</sup> Evaluation of measured spectra was performed by the PosWin code using SiC as a reference material.<sup>42</sup> Positron annihilation spectra measured at different positron energies were decomposed into three characteristic lifetime components  $\tau_1$ ,  $\tau_2$ ,

and tau-3. Each of these components is characterized by a given intensity I-1, I-2, I-3, depending on the positron annihilation rate of each specific defect type. In general, tau-1 corresponds to the bulk lifetime (107 ps in a defect-free Fe matrix). In most cases, however, the measured tau-1 value is a mixture of bulk lifetime and extended positron traps (e.g., dislocations or particle/matrix interfaces), associated with a shorter lifetime. Components tau-2 and tau-3 are lifetime contributions due to (small) defect populations, having their own characteristic sizes and number densities. *Ab initio* calculations and measurements have shown that ODS particle/matrix interfaces have a strong affinity with diffusing positrons.<sup>43</sup> For this reason, the mean positron lifetime MLT evolutions, including tau-1, tau-2, and tau-3 contributions, are mainly attributed to open volume variations taking place at particle/matrix interfaces, where cavitation has been directly evidenced.<sup>19,21</sup>

### 5. Experimental methods: General discussion

The present study attempts to link the micro-mechanical response of three different ODS alloys with their corresponding, dose-dependent microstructural evolutions. For practical reasons, our approach combines experimental results representing different portions or depth ranges of the implanted/irradiated region (see Fig. 1). For instance, the TEM observations are carried out in thin foils cut out of the near-surface region (0–200 nm), for simplicity and experimental repeatability; whereas the PLEPS measurements are partially probing the He-implantation range (300–550 nm). The combination of TEM and PLEPS results provide complementary yet consistent evidence; which allows us to rationalize the dose-dependent particle size and number density evolutions as explained in Sec. V A.

The indent-induced plastic zone in contrast extends through the entire damage layer thickness (up to  $\sim 2.2\ \mu\text{m}$  depth) given the selected indenter displacement (up to 500 nm). The dose-dependent evolutions of the indentation response are nonetheless significant (cf. Tables IV and V), repeatable, and consistent with the observed microstructural changes (cf. Fig. 4 and Table III), whereas the influence of the undamaged substrate is kept minimal (The indent-induced plastic zone extent is up to —four to five times the indenter penetration depth.). We thus assume that the top 550 nm zone («TEM» and «PLEPS» marked regions in Fig. 1) is fairly representative of the entire damaged zone ( $\leq 2.2\ \mu\text{m}$  depth), at least in terms of indent-induced plasticity mechanisms (see Refs. 20 and 34 and Sec. IV B 3). This situation enables us to rationalize Table IV and Figs. 5–7 measurements as explained in Secs. V B and V C.

## IV. EXPERIMENTAL RESULTS

### A. As-received alloys

Nano-indentation data associated with the as-received material are presented together with post-irradiation data in Sec. IV B 3, for the sake of clarity.

#### 1. ODS particle size distribution: SANS and TEM observations

The SANS measurements are adjusted assuming a dual particle size distribution (see Table II and Fig. 2). The smaller particles are up to two orders of magnitude more numerous than the larger

**TABLE II.** As-received particle size distributions in ODS-1, ODS-2, and ODS-3 alloys based on SANS data analysis and TEM observations. SANS data are analyzed assuming a dual particle size distribution including «small» and «large» particles. The results corresponding to each case are placed into separate columns. The TEM data focus on the particles smaller than 20 nm.

		SANS (small)	SANS (large)	TEM
ODS-1	D	$5 \pm 1.0\ \text{nm}$	$16 \pm 1.0\ \text{nm}$	$15.1 \pm 0.6\ \text{nm}$
	$N_p$	$2 \times 10^{17}\ \text{cm}^{-3}$	$4 \times 10^{15}\ \text{cm}^{-3}$	$4 \times 10^{15}\ \text{cm}^{-3}$
ODS-2	D	$4 \pm 1.0\ \text{nm}$	$13 \pm 1.0\ \text{nm}$	$7.3 \pm 0.4\ \text{nm}$
	$N_p$	$6 \times 10^{16}\ \text{cm}^{-3}$	$6 \times 10^{14}\ \text{cm}^{-3}$	$4 \times 10^{16}\ \text{cm}^{-3}$
ODS-3	D	$5 \pm 1.0\ \text{nm}$	$12 \pm 1.0\ \text{nm}$	$9.2 \pm 0.9\ \text{nm}$
	$N_p$	$5 \times 10^{17}\ \text{cm}^{-3}$	$1 \times 10^{16}\ \text{cm}^{-3}$	$3 \times 10^{16}\ \text{cm}^{-3}$

ones. A regular distribution of  $\text{Y}_2\text{O}_3$  particles embedded in a pure Fe matrix corresponds to a theoretical scattered intensity ratio  $A_{\text{th}} = 2.95$ . A homogeneous distribution of  $\text{Y}_2\text{Ti}_2\text{O}_7$  in a pure Fe matrix yields  $A_{\text{th}} = 2.45$ . A homogeneous distribution of oxygen-rich  $\text{Y}_2\text{Ti}_2\text{O}_7$  particles in a pure Fe-14Cr matrix corresponds to  $A_{\text{th}} = 2.54$ , whereas oxygen-poor  $\text{Y}_2\text{Ti}_2\text{O}_3$  particles correspond to  $A_{\text{th}} = 2.95$ . The actual neutron scattering intensity ratios obtained in ODS-1, ODS-2, and ODS-3 are  $A = 2.8, 2.5,$  and  $2.4,$  respectively. ODS-1 result is consistent with a mix of oxygen-poor  $\text{Y}_2\text{O}_3$  particles and small cavities (2.8 vs 2.95). ODS-2 and ODS-3 results are consistent with oxygen-rich particles  $\text{Y}_2\text{TiO}_5$  or  $\text{Y}_2\text{Ti}_2\text{O}_7$  (2.5 and 2.4 vs 2.54). The difference between measurements and theoretical values possibly indicates the incomplete mixing of the  $\text{Y}_2\text{O}_3$  into the ferrite matrix, due to the relatively short milling time adopted. The chemical composition of ODS-2 and ODS-3 particles cannot be uniquely determined based on the present evidence, however. It is nonetheless important to note that both  $\text{Y}_2\text{Ti}_2\text{O}_7$  (orthorhombic) and  $\text{Y}_2\text{TiO}_5$  (FCC) particle cases yield incoherent interfaces, with respect to the BCC Fe (or Fe–Cr) matrix. Incoherent ODS-2 and ODS-3 particles make much stronger obstacles to mobile dislocations than coherent ODS-1 particles do (see Sec. V B).

The theoretical scattered intensity ratio corresponding to a homogeneous distribution of nano-cavities embedded in a pure Fe matrix is  $A_{\text{th}} = 1.34$ . Signal scattering due to porosities is, therefore, not present, given the above-reported «A» ratios. SANS measurements are consistent the following particle volume fractions  $f = 0.8\%, 1.8\%, 2.2\%$  in ODS-1, ODS-2, and ODS-3, respectively. The larger particle distributions are broadly consistent with TEM-based particle counts, in ODS-1, 2, and 3. Refinement in the nano-particle size is observed upon Ti addition. Cr addition does not induce any significant change in terms of the initial nano-particle size distribution (viz., ODS-2 and ODS-3). The present SANS (Fig. 2) vs TEM result comparison (Table II) confirms, first, the long-range uniformity of particle dispersions in our model alloy fabrications and second, validates our particle counting method based on TEM imaging, at least for particle sizes larger than 5 nm. Complementary EELS analysis in ODS-2 and ODS-3 (not shown) indicate that Ti is mostly located within the particles; while Cr (in ODS-3) is present in both the particles and the matrix.

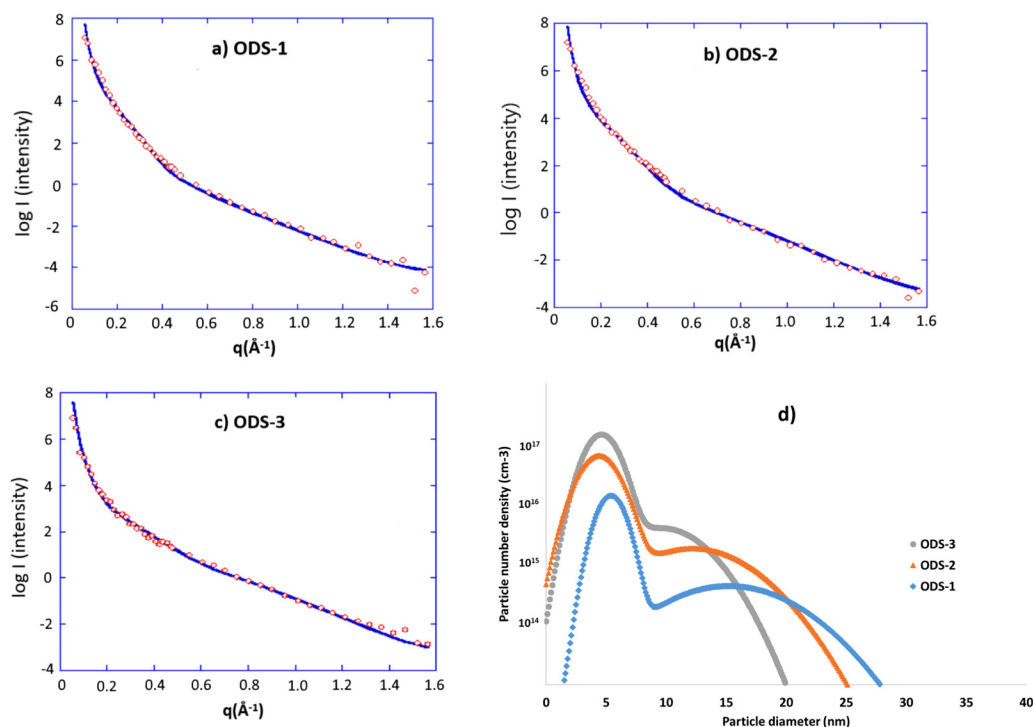


**FIG. 2.** SANS experiments: direct and indirect measurements. SANS intensity evolution with scattering vector «q» in (a) ODS1, (b) ODS-2, (c) ODS-3. (d) Corresponding particle size distributions in ODS-1, ODS-2, and ODS-3. The analysis of the SANS scattering curves is carried out assuming a dual particle size distribution.

## 2. ODS particle crystallographic structure: HRTEM

Some of the observations reported in this section have been presented elsewhere<sup>21</sup> and are briefly recalled here (see Fig. 3), for the sake of clarity and completeness. High-resolution TEM (HRTEM) observations reveal that the crystallographic structure of the particles strongly depends on the alloy chemical composition, for instance,

1. ODS-1 alloy (Fe-0.3Y<sub>2</sub>O<sub>3</sub>) contains Y<sub>2</sub>O<sub>3</sub> particles of the BCC crystallographic structure. In that case, the particle/matrix interface is fully coherent (see Fig. 3 in Ref. 19 and Fig. 5 in Ref. 21).
2. ODS-2 alloy (Fe-0.2Ti-0.3Y<sub>2</sub>O<sub>3</sub>) nanoparticles are compatible with Y<sub>2</sub>TiO<sub>5</sub> or Y<sub>2</sub>Ti<sub>2</sub>O<sub>7</sub> stoichiometry and non-BCC crystallographic structure.
3. ODS-3 alloy (Fe-14Cr-0.2Ti-0.3Y<sub>2</sub>O<sub>3</sub>) nanoparticle characteristics are comparable to those of ODS-2.

The ODS-2 and ODS-3 particles are incoherent relative to the bcc matrix and include misfit dislocations (not shown). The present HRTEM observations are consistent with SANS data, in terms of particle stoichiometry (see Sec. IV A 1).

## B. Post-irradiation experimental analysis

### 1. TEM and HRTEM observations

All the TEM observations reported in this section are carried out in thin foils cut from the near-surface region (<200 nm), where

the damage level  $\sim 40$  dpa and the corresponding peak damage level  $\sim 150$  dpa (see Sec. III B and Table I). Non-ODS (particle-free) Fe and Fe–Cr alloys irradiated up to  $\sim 40$  dpa at  $T_{irr} = 500$  °C typically include TEM-resolved defect cluster dispersions, in the form of dislocation loops.<sup>44–46</sup> Such loop (or void) populations were not detected in post-irradiated ODS-1, ODS-2, and ODS-3 alloys subjected to  $T_{irr} \geq 500$  °C, whatsoever.<sup>19</sup> This finding indicates that the presence of ODS particles significantly augments the recombination rate of (radiation-induced) migrating point defects, that would otherwise contribute to the growth of TEM-resolved defect clusters, in the matrix region. The main radiation-induced microstructural evolutions regard the particle size distributions, as described hereinafter.

- ODS-1: small (<5 nm) and large (>20 nm) particles are partially dissolved after 40 dpa at  $T_{irr} = 500$  °C. The average particle size, thus comes down from 15 nm to 9 nm. A similar, more pronounced evolution has been reported in post-irradiated ODS-1, after 25 dpa at  $T_{irr} = 600$  °C.<sup>20,21</sup>
- ODS-2: a slight particle refining effect is observed: the majority of the small particles survive the irradiation, whereas the larger particles are (at least partially) dissolved (see Fig. 5 from Ref. 19).
- ODS3: particle refining is more pronounced than in ODS-2. Particle refining intensity is irradiation-temperature dependent, being more pronounced at  $T_{irr} = 700$  °C than  $T_{irr} = 600$  °C (see Table III). After irradiation at 700 °C, however, particle size

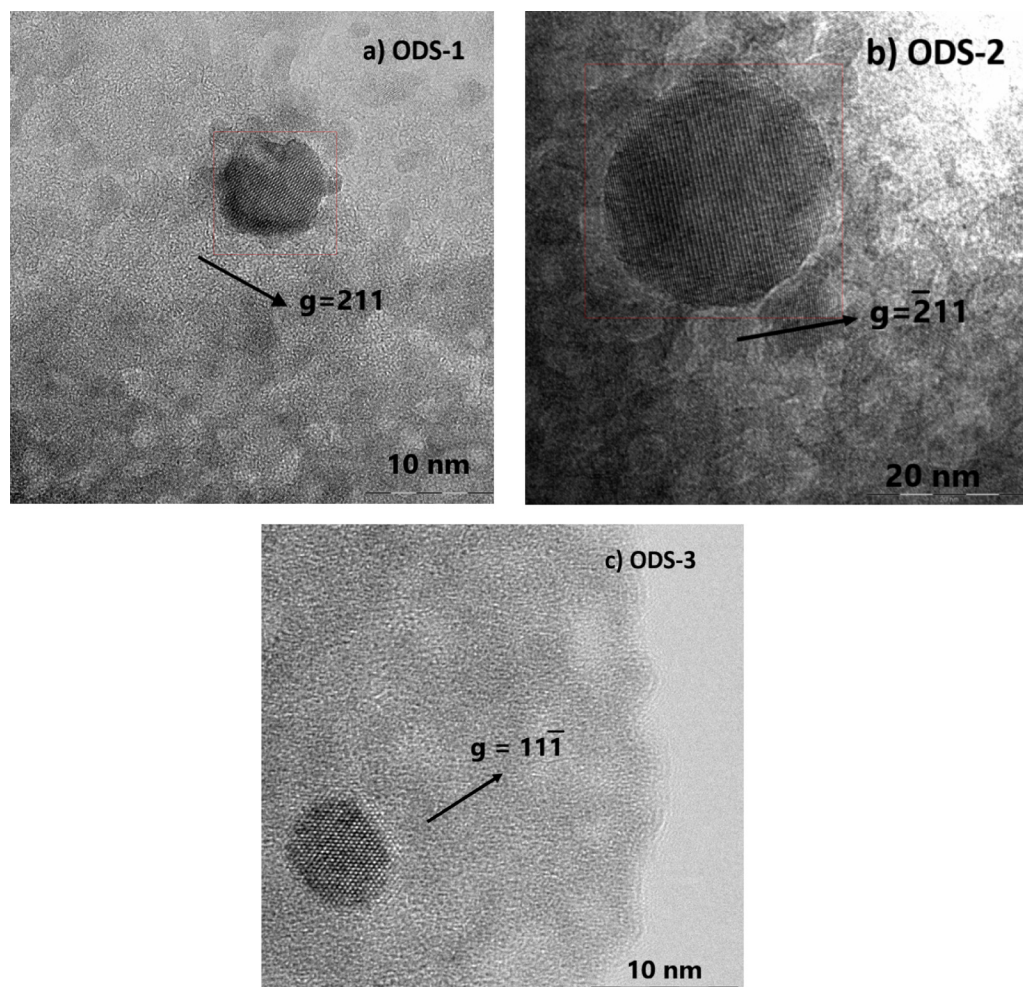


**FIG. 3.** HRTEM micrographs of typical ODS particles in as-received model alloys. In (a) ODS-1, (b) ODS-2, and (c) ODS-3. ODS-1 particles have a BCC crystallographic structure (see the main text), in contrast with ODS-2 and ODS-3 particles. Misfit dislocations (not shown) are present at both ODS-2 and ODS-3 particle/matrix interfaces.

evolution may significantly differ from one location to another. In a few cases, small cavities or voids seemingly attached to surviving particles are directly evidenced.

HRTEM observations show that the ODS particles remain mostly crystalline, after irradiation up to 600 °C. The effect of

particle size evolution on the micro-mechanical response of the steels is presented below, in Sec. IV B 3.

## 2. Positron annihilation analysis

Positron lifetime evolutions are measured at specific specimen depths comprised between 300 and 525 nm (see Fig. 4),

**TABLE III.** Average ODS particle size associated with 40 dpa damage level accumulated at different irradiation temperatures. The data are based on TEM examinations and focus on the fine particles (smaller than 20 nm). Post-irradiation particle size histograms are available in Fig. 5 of Ref. 19 for irradiation temperatures 600 and 700 °C.

Irradiation $T^\circ$	500 °C		600 °C		700 °C
Alloy	ODS-1	ODS-2	ODS-3	ODS-2	ODS-3
D (nm)	9	5	4,7	5	1–4
$N_p$ (cm <sup>-3</sup> )	$1.0 \times 10^{17}$	$3.5 \times 10^{16}$	$5.0 \times 10^{17}$	$3.8 \times 10^{16}$	$4.0 \times 10^{17}$



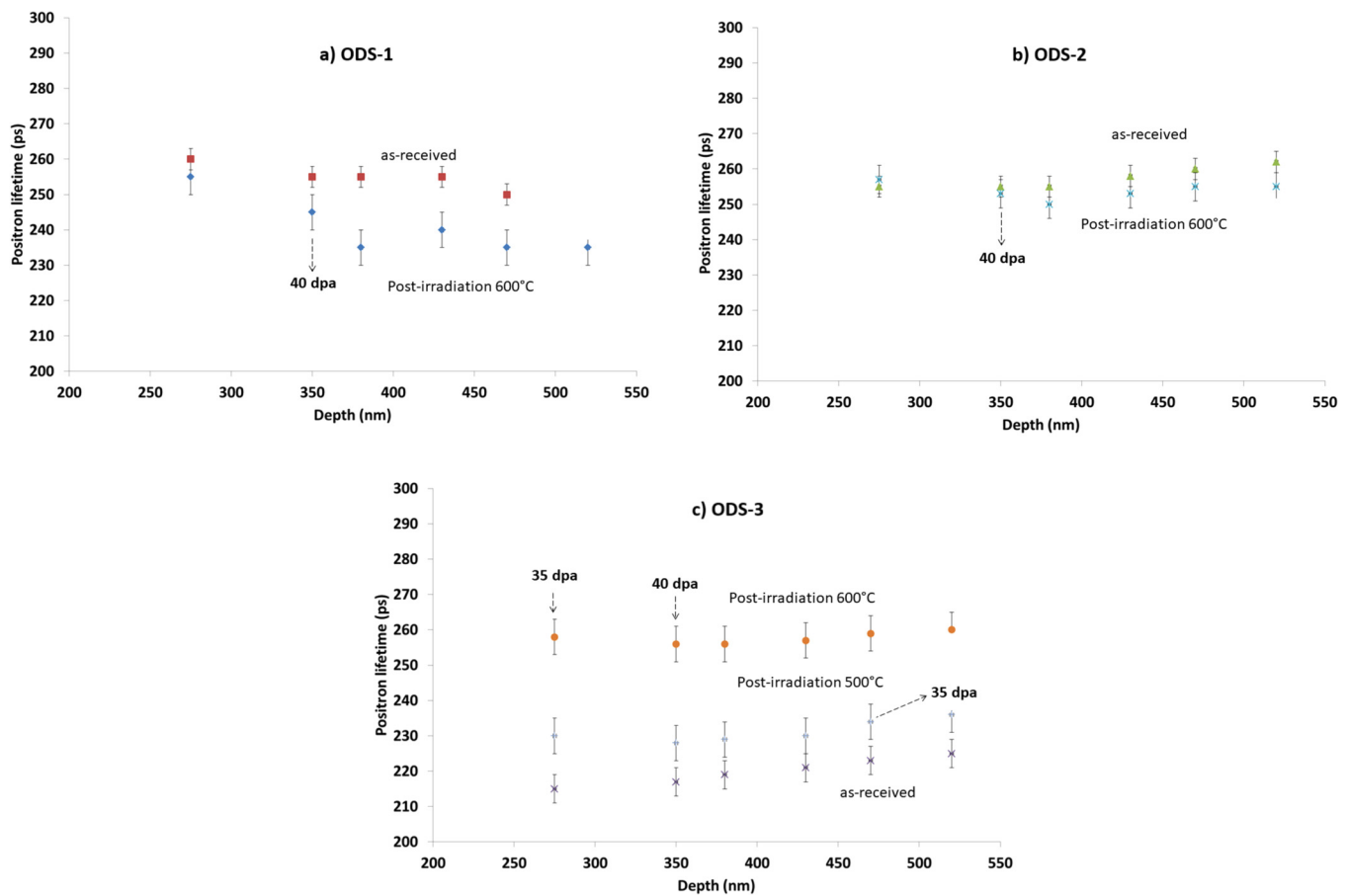


**FIG. 4.** Positron lifetime measured at different depths, before and after irradiation. The damage level increases with respect to the depth normal to the specimen surface, along the ion implantation peak. (a) ODS-1: the post-irradiation, mean positron lifetime is lower than in as-received conditions. A constant lifetime decrease of 20 ps is obtained beyond 370 nm depth. (b) ODS-2: the mean post-irradiation positron lifetime evolution is small, regardless of the positron implantation depth, i.e., regardless of the dose level < 40 dpa. (c) ODS-3: initial mean positron lifetime is lower than in ODS-1 and ODS-2 [see Figs. 4(a) and 4(b)]; however, the lifetime significantly augments with the irradiation damage and temperature.

corresponding to the positron implantation depths. The initial mean lifetimes (MLT) measured at 375 nm depth are 255 ps in ODS-1; 255 ps in ODS-2, and 220 ps in ODS-3. Defect lifetime contribution  $\tau$ -2 is about 360–420 ps consistent with 15–25 sized vacancy clusters.<sup>47</sup> Corresponding intensity I-2 = 30% in ODS-1 and ODS-2, whereas I-2 = 20% in ODS-3. Intensity I-2 drop in ODS-3 is likely due to the chromium alloying element, as there was no major difference in  $\tau$ -2 lifetimes and I-2 intensities of ODS-1 and ODS-2, differing only by 0.2% added titanium. Defect lifetime  $\tau$ -3 corresponds to intensity I-3 differs by about two orders of magnitude compared to intensities I-1 and I-2. For this and other reasons,  $\tau$ -3 and I-3 values are no further reported, in the rest of the paper.

The significant dose-dependent MLT evolutions (at 375 nm depth) include in ODS-1, the mean positron lifetime drops (–15 ps) after irradiation at 600 °C. The lifetime measured beyond 370 nm depth (i.e., up to 45 dpa) is mostly constant. The positron lifetime

contributions  $\tau$ -1 and  $\tau$ -2 measured at 375 nm are 90 and 270 ps, with corresponding intensities 22% (intensity I1) and 62% (intensity I2). In ODS-2, the mean positron lifetime after irradiation at 600 °C is almost constant at all measured depths and corresponding dose levels (–10 ps: within the error bars). Positron lifetimes  $\tau$ -1 and  $\tau$ -2 measured at 375 nm are 70 and 240 ps, with corresponding intensities 25% (intensity I1) and 70% (intensity I2).

In ODS-3, the mean positron lifetime rises by +10 ps after irradiation at 500 °C and by +40 ps after irradiation at 600 °C. The mean positron lifetime thus significantly depends on the irradiation temperature, in the 35–45 dpa damage range. The positron lifetime contributions  $\tau$ -1 and  $\tau$ -2 measured at 375 nm are 120 and 290 ps, with corresponding intensities 30% (intensity I1) and 70% (intensity I2).

The post-irradiation  $\tau$ -2 lifetimes range from 250 to 300 ps, which is consistent with 5–10 vacancy clusters sitting next to yttrium oxides particles (~240 ps).<sup>48</sup> Positron lifetime  $\tau$ -2

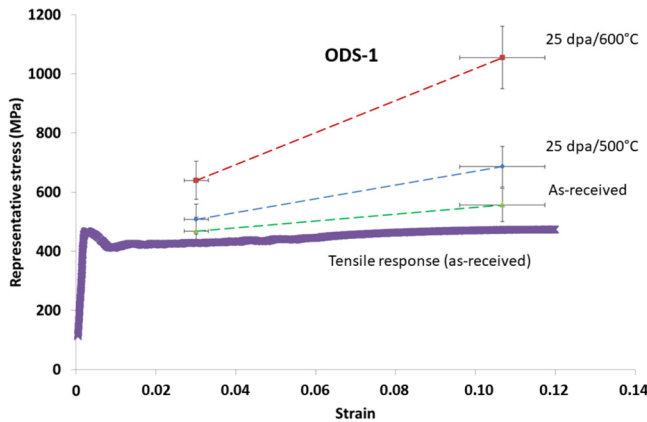


**FIG. 5.** Room-temperature response of ODS-1 before and after irradiation. The micro-mechanical tensile data are plotted along with macroscopic reference tensile data (as-received condition), for comparison. The onset of macroscopic plasticity shows heterogeneous strain development (<1% strain), followed by a stable parabolic hardening regime, at higher plastic strain levels (>1% strain). In ODS-1, a pronounced dose-dependent evolution of the micro-work-hardening response is evidenced, with increasing irradiation temperature. The indicated damage levels (in dpa) are the reference near-surface values, from Table I.

increases from about 250 ps at 430 nm depth to about 300 ps at

500 nm depth, which represents a defect cluster size increase by a factor 2. This effect may correspond to 5–10 vacancy clusters including one to three helium atoms,<sup>49,50</sup> consistent with the He-implantation profile as shown in Fig. 1.

### 3. Nano-indentation measurements and analysis

*a. Nano-indentation testing at room temperature without dwell time.* Nano-indentation is used to evaluate the irradiation-induced effect on the micro-mechanical response of the steels. The recorded load-displacement curves are analyzed using a specific, alternate method, yielding an equivalent micro-tensile response consistent with the indentation test results.<sup>20,35,36</sup> The obtained stress-strain response is generally not directly comparable to the macroscopic tensile data, although it may help reveal important changes taking place at the subgrain scale. Analysis of the indentation data is based on fitting the loading part of the indentation curve with  $P = C_\theta h^2$ , where  $P$  is the applied force,  $C_\theta$  is the «curvature» parameter, and  $h$  is the indenter penetration depth.

The curvature parameters obtained using two indenter geometries (Berkovich and cube-corner) are listed in Table IV for different experimental conditions (see Table I). To each curvature parameter  $C_\theta$  in Table IV and indenter included angle  $\theta$  corresponds representative stress  $\sigma_{r\theta}$  and strain  $\epsilon_{r\theta}$ ,<sup>36</sup> where

$$\epsilon_{r\theta} = 0.105 \cot \theta, \tag{1}$$

$$\frac{C_\theta}{\sigma_{r\theta}} = \tan^2 \theta \left\{ 0.02552 \left[ \ln \left( \frac{E^*}{\sigma_{r\theta}} \right) \right]^3 - 0.72526 \left[ \ln \left( \frac{E^*}{\sigma_{r\theta}} \right) \right]^2 + 6.34493 \left[ \ln \left( \frac{E^*}{\sigma_{r\theta}} \right) \right] - 6.47458 \right\}. \tag{2}$$

Bulk modulus  $E^* = 220$  Gpa is measured from the unloading part of the indentation curve. Reference stress-strain values ( $\sigma_{r\theta}$ ,  $\epsilon_{r\theta}$ ) are extracted from the tensile curve in Fig. 5 and then

adjusted with Eqs. (1) and (2) using  $C_\theta$  amounts associated with the indenter geometry considered (Berkovich or cube-corner). In practice, we applied the following, three steps calculation

**TABLE IV.** Curvature parameter fitting the loading part of the nano-indentation curves for Berkovich ( $C_\theta$ -Berk) and Cube-corner ( $C_\theta$ -cc) indenter geometries. Each  $C_\theta$  value specified denotes data scattering associated with up to 50 different indentation curves. In practice, the  $\pm$  margins correspond to an interval including over 90% of the measured  $C_\theta$  «curvature» parameters, expressed in mN/nm<sup>2</sup> units. All the indentation tests are conducted at room temperature. The indicated damage levels (in dpa) are the reference near-surface values, from Table I.

Irradiation $T^\circ$	As-received conditions	ODS-1			
		500 °C 25 dpa	25 dpa	600 °C 40 dpa	700 °C 40 dpa
$C_\theta$ -Berk	$(6.0 \pm 0.2) \times 10^{-5}$	$(6.0 \pm 0.1) \times 10^{-5}$	$(7.5 \pm 0.1) \times 10^{-5}$	...	...
$C_\theta$ -cc	$(7.0 \pm 0.1) \times 10^{-5}$	$(8.0 \pm 0.1) \times 10^{-6}$	$(1.2 \pm 0.1) \times 10^{-5}$	...	...
		ODS-2			
$C_\theta$ -Berk	$(7.0 \pm 0.5) \times 10^{-5}$	$(7.2 \pm 0.5) \times 10^{-5}$	$(7.1 \pm 0.5) \times 10^{-5}$	...	...
$C_\theta$ -cc	$(9.0 \pm 0.4) \times 10^{-6}$	$(9.2 \pm 0.4) \times 10^{-6}$	$(8.9 \pm 0.4) \times 10^{-6}$	...	...
		ODS-3			
$C_\theta$ -Berk	$(9.0 \pm 0.4) \times 10^{-5}$	...	...	$(9.0 \pm 0.4) \times 10^{-5}$	$(9.0 \pm 0.4) \times 10^{-5}$
$C_\theta$ -cc	$(1.1 \pm 0.5) \times 10^{-5}$	...	...	$(1.0 \pm 0.5) \times 10^{-5}$	$(1.2 \pm 0.5) \times 10^{-5}$

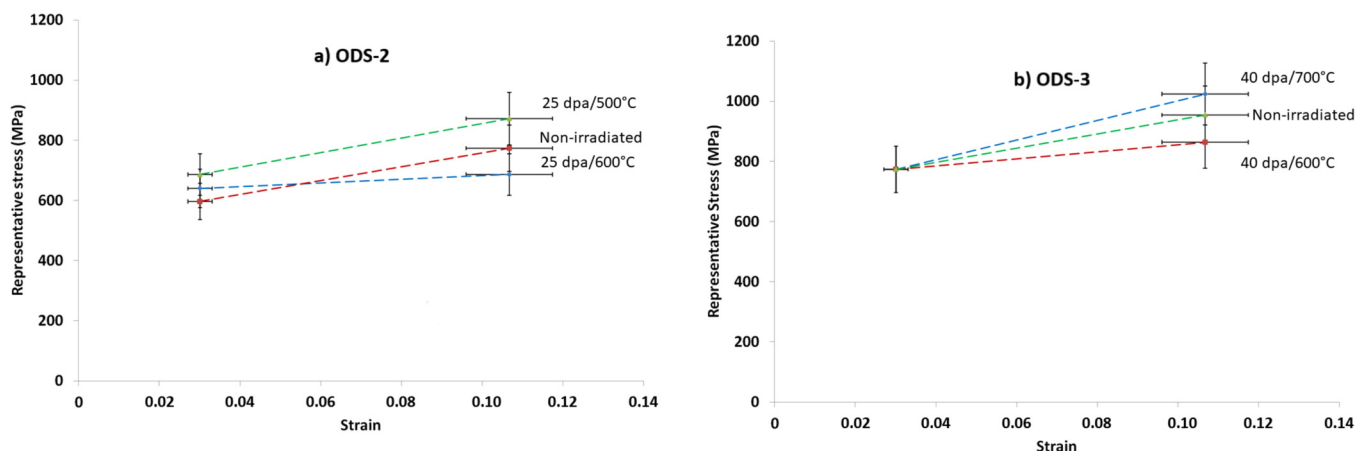


**FIG. 6.** Nano-indentation response at room temperature in ODS-2 and ODS-3, before and after irradiation. (a) In ODS-2, no significant irradiation-induced changes are observed, up to 25 dpa at 600 °C. (b) In ODS-3, no significant irradiation-induced changes observed, up to 40 dpa at 700 °C. The indicated damage levels (in dpa) are the reference near-surface values, from Table I.

procedure. Step-1, we make a first estimate of  $\varepsilon_{r\theta}$  strain using Eq. (1) taking the constructor-specified  $\theta$  angle for a given indenter geometry. Step-2, we find the  $\sigma_{r\theta}$  level corresponding to  $\varepsilon_{r\theta}$  (from Step-1) in consistency with the reference tensile curve of Fig. 5. Step-3, we solve the resulting expressions for  $\theta$  using the appropriate  $C_\theta$  value, representative of the un-irradiated material condition (from Table IV). This procedure allows finding the precise, effective aperture angle of each indenter, to be used for the different evaluations presented in Figs. 5 and 6.

The reference stress-strain (tensile) curve of Fig. 5 is obtained by monitoring the elongation of a macroscopic (as-received) ODS-1 specimen against the applied force, accounting for the compliance correction of the tensile stage. The tensile specimen gauge section dimensions are  $12 \times 4 \times 1 \text{ mm}^3$ . The macroscopic tensile strain is applied at constant strain rate  $5 \times 10^{-4} \text{ s}^{-1}$  up to 12% plastic deformation. The corresponding maximum applied load is 1330 N, whereas the estimated yield stress is 413 MPa and the ultimate tensile is 474 MPa.

The initial yield point clearly depends on the alloy composition, from  $\sigma_R \approx 450 \text{ MPa}$  in as-received ODS-1 (Fig. 5), up to  $\sigma_R \approx 800 \text{ MPa}$  (Fig. 6) in as-received ODS-3. In ODS-1, the co-implanted helium has a systematic and significant influence on the initial yield point, up to about 600 MPa after 25 dpa at  $T_{irr} = 600 \text{ °C}$ . For a fixed irradiation dose, the (micro) work-hardening response of ODS-1 markedly increases with the irradiation temperature (see Fig. 5). Conversely, the micro-mechanical work-hardening response of ODS-2 and ODS-3 is mostly stable and dose-independent, regardless of  $T_{irr}$  (see Fig. 6). A stable micro-tensile response is concurrent with good particle tolerance to radiation-induced effects (see Sec. V B).

*b. Indentation testing with dwell time at room and elevated temperature.* The indentation experiments involve specific straining mechanisms (see Sec. V B), to be investigated at different stabilized temperatures:  $T_{dwell} = 25, 100, 400, \text{ or } 500 \text{ °C}$ . The indenter is

pressed toward the specimen surface at the constant loading rate of 1.0 mN/s, up to a fixed applied force of 20 mN. This load corresponds to an initial indenter penetration depth of about 500 nm. The applied load is then kept constant (20 mN) during 1200 s, while the indenter displacement is continuously recorded. We found that the micro-creep response in ODS-3 is mostly temperature-independent, after irradiation to 25 dpa at  $T_{irr} = 500 \text{ °C}$  (see Fig. 7).

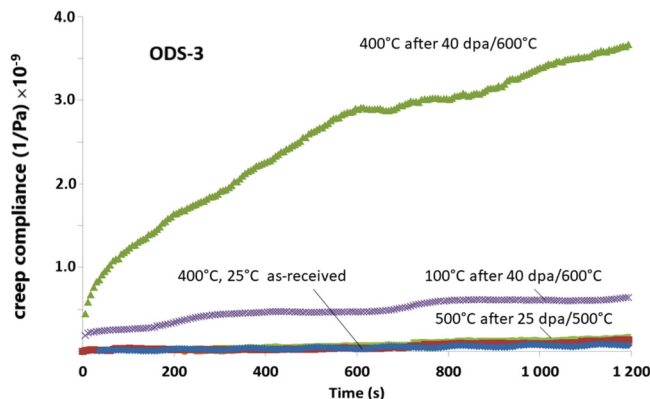


**FIG. 7.** Indentation creep response at various test temperatures in ODS-3, before and after irradiation. The creep compliance data correspond to  $\dot{\varepsilon}t/\sigma_{cl}$  expressed in  $\text{Pa}^{-1}$  units, where  $\dot{\varepsilon}$  is the creep rate ( $\text{s}^{-1}$ ),  $t$  is the time (s), and  $\sigma_{cl}$  is the climb stress (Pa). In the selected test conditions, we estimate that the 20 mN applied load gives rise to a representative indent-induced stress magnitude  $\sigma_{cl} \approx \sigma_R \sim 800 \text{ MPa}$  [see Fig. 6(b)]. It is found that the indentation creep rate at 400 °C is mostly dose-independent, after irradiation up to 25 dpa at 500 °C. The indicated damage levels (in dpa) correspond to the reference near-surface values listed in Table I.

**TABLE V.** Indentation creep response of ODS-3 at different temperatures, in as-received and irradiated conditions. The creep compliance (in  $\text{Pa}^{-1}$ ) and corresponding creep rate ( $\text{s}^{-1}$ ) values indicated are measured at  $t = 1200$  s. The tests were conducted at different temperatures, from  $25^\circ\text{C}$  up to  $500^\circ\text{C}$ . The indicated damage levels (in dpa) correspond to the reference near-surface values, from Table I.

Creep test $T^\circ$	$25^\circ\text{C}$	$100^\circ\text{C}$	$400^\circ\text{C}$	$500^\circ\text{C}$
0 dpa	$5.8 \times 10^{-11} \text{ Pa}^{-1}$ $3.9 \times 10^{-5} \text{ s}^{-1}$	...	$1.8 \times 10^{-10} \text{ Pa}^{-1}$ $1.2 \times 10^{-4} \text{ s}^{-1}$	...
25 dpa/ $500^\circ\text{C}$	$4.4 \times 10^{-11} \text{ Pa}^{-1}$ $2.9 \times 10^{-5} \text{ s}^{-1}$	...	...	$9.6 \times 10^{-11} \text{ Pa}^{-1}$ $6.4 \times 10^{-5} \text{ s}^{-1}$
40 dpa/ $600^\circ\text{C}$	$3.9 \times 10^{-11} \text{ Pa}^{-1}$ $2.6 \times 10^{-5} \text{ s}^{-1}$	$6.5 \times 10^{-10} \text{ Pa}^{-1}$ $4.3 \times 10^{-4} \text{ s}^{-1}$	$3.6 \times 10^{-9} \text{ Pa}^{-1}$ $2.4 \times 10^{-3} \text{ s}^{-1}$	...

The micro-creep response has a strong temperature dependence, after irradiation to 40 dpa at  $T_{\text{irr}} = 600^\circ\text{C}$ . For instance, the creep compliance measured at  $T_{\text{dwell}} = 400^\circ\text{C}$  is up to 20 times larger than that measured at  $T_{\text{dwell}} = 25^\circ\text{C}$  (see Fig. 7 and Table V), for a given dwell time. These evolutions are further discussed in Sec. V B based on TEM, HRTEM, PAS, and PLEPS observation results combined.

## V. DISCUSSION

### A. On the irradiation-induced ODS particle evolutions

It is assumed that the large particles ( $>10$  nm) have little effect on the post-irradiation micro-mechanical response, given their large spacing with respect to the indent-induced plastic zone size. The rest of the discussion thus focuses on the fine particle evolutions. Two different particle-size evolution trends are hereinabove documented:

1. In ODS-1, the fine particles are partially dissolved during the irradiation, and the particle loss intensity depends on the irradiation temperature, for a given irradiation dose.
2. In ODS-2 and ODS-3, the fine particles are mostly stable, regardless of the dose/temperature irradiation conditions applied.

These evolution trends are interpreted as follows. The point defect sink strength of the particle/matrix interface scales with the particle/matrix misfit energy.<sup>46</sup> The sink strength of coherent ODS-1 particle interfaces should then be significantly weaker than the sink strengths of incoherent ODS-2 and ODS-3 particle interfaces (see Sec. IV A 2). For this reason, point defects (vacancies and interstitials) generated inside ODS-1 particles can easily cross the particle/matrix interfaces and end up diffusing away, toward the surrounding matrix. Such outgoing defects (especially, O and Y interstitial atoms) quickly recombine thereof, given their strong affinity with the matrix vacancies.<sup>51,52</sup> In ODS-1, the positron lifetime markedly decreases with the dose indeed [see Fig. 4(a)]. This means the vacancy flux balance in the particle/matrix interface is somewhat negative and concurrent with a high defect recombination rate in the matrix. The combination of weak particle/matrix sink strength and high matrix defect recombination rates are both consistent with a relatively fast particle dissolution rate, in the dose/temperature range investigated herein.

In ODS-2, the initial positron lifetime is significantly larger than in ODS-1 and ODS-3 and exhibits a minimal dose-

dependence [see Fig. 4(b)]. This means that the vacancy flux balance (inbound/outbound) in the particle/matrix interface is seemingly stable and has practically no effect on the particle/matrix interface topology. This condition is concurrent with particle stability and indicates that point defects (Y and O interstitials, in particular) generated inside ODS-2 particles have limited mobility, at least up to 40 dpa and  $T_{\text{irr}} = 600^\circ\text{C}$ . Recombination of outbound point defects with matrix defects may nonetheless take place, under more stringent dose/temperature conditions.<sup>52,53</sup>

In ODS-3, the positron lifetime significantly increases with the dose and irradiation temperature [Fig. 4(c)], indicating a positive vacancy flux balance, in the particle/matrix interface. Incidentally, the addition of Cr into a Fe matrix reduces the vacancy formation energy and/or increases the vacancy migration energy. This effect limits the point defect recombination rate inside the matrix,<sup>54</sup> thereby fostering point defect accumulation at the particle/matrix interface. Strong particle/matrix interfacial sink strength and a relatively low matrix defect recombination rate are both concurrent with relatively good particle resistance to radiation-induced dissolution, at least up to 40 dpa and  $T_{\text{irr}} = 700^\circ\text{C}$ .

The particle size evolutions documented in this study are consistent with the high-temperature regime prescribed in Refs. 55 and 56, where thermally activated diffusion dominates the ballistic effects. The BCC particle structure in ODS-1 markedly differs from the orthorhombic particle structure observed in ODS-2 and ODS-3. Such disparity influences the thermally driven migration of point defects to and from the particle/matrix interfaces and then, possibly explains the broader dose-temperature stability domain of ODS-2 and ODS-3, compared to ODS-1. Detailed APT studies showed Cr shells are present around oxide particles of all sizes in the ODS-3 alloy.<sup>21,57</sup> The core/shell particle structuration enables pronounced dose-dependent evolutions of ODS-3 particle/matrix topology (sink strength) and moderate dose-dependent evolutions of ODS-1 and ODS-2 particle topology, devoid of a Cr shell. The observed trend is in any case the reduction of the particle O-content with increasing  $T_{\text{irr}}$ , where the Cr shell becomes less distinct and bears a lower Cr concentration. Finally, the implanted helium atoms have strong affinity with small (5–10) vacancy clusters, as reported in Sec. IV B 2. Implanted helium atoms then possibly affect particle stability (i) by altering the small (5–10) vacancy cluster sink strength and (ii) by affecting the mobility of isolated, incoming vacancies.

## B. Indentation response without dwell time

Two different post-irradiation evolution trends are evidenced,

1. In ODS-1, the work-hardening response is strongly dose-dependent. This effect is concurrent with pronounced dissolution of the finer particles, decreasing the open volume at particle/matrix interfaces [see Fig. 4(a)] and partial particle amorphization.
2. In ODS-2 and ODS-3, the work-hardening response is mostly stable, regardless of the irradiation conditions applied. The fine particles are stable with cumulated irradiation damage, in association with a stable or increasing open volume at particle/matrix interfaces [see Figs. 4(b) and 4(c)].

Correlation between the particle size evolution and the micro-mechanical response can be rationalized as follows.

### 1. In as-received condition

Plastic strain spreading in ODS grains involves the creation of numerous wavy slip (or shear) bands. In these conditions, the local (grain-scale) work-hardening rate mainly depends on the gradual build-up of dislocation pileups or tangles, at the grain boundaries. The work-hardening rate associated with this mechanism depends on the number of mutually interacting slip bands per unit grain volume.<sup>58</sup> Mobile dislocations can generally not cut through the oxide particles, especially if the particle/matrix interface is incoherent, as in ODS-2 and ODS-3 cases.<sup>59</sup> As a result, dislocation/particle interactions involve dislocation and dislocation debris accumulation, near the ODS particles. These conditions help spread the (new) incoming dislocations out of their initial glide planes through the cross-slip mechanism, thus generating multiple secondary slip bands. In these conditions, the mutual slip band interaction is strong, yielding a much weaker (micro) work-hardening response than ODS-1 does.<sup>34,58</sup>

### 2. In post-irradiation condition

The ODS particle size distribution is dose-dependent (especially, in ODS-1, see Sec. IV B 1). Dissolution of the finer particles fosters strain localization, which then decreases the number of strain-induced slip bands for a given grain size and plastic strain level.<sup>34,58</sup> A lower slip band number density yields limited band/band, mutual elastic interactions. In these conditions, the grain-scale work-hardening rate increases with the dose as shown in Fig. 5. Decreasing the fine particle number density in ODS-1 yields qualitatively the same effect as depressing the straining temperature (Depressing the straining temperature also depresses the cross-slip probability and, therefore, plastic strain spreading uniformity, across the strained grains.), in typical un-irradiated homogeneous (non-ODS) alloys.<sup>60</sup> The distinct (relatively minor) particle-size distribution evolutions in ODS-2 and ODS-3 yield the stable indentation response, as shown in Fig. 6.

## C. Indentation response with dwell time

### 1. General ideas: Indentation creep mechanism in ODS-3 alloy

It is important to note that indentation experiments involve dislocation nucleation near the tip of the indenter and therefore,

very high local dislocation densities.<sup>61</sup> In conventional creep tests, such conditions are typically found at the end of the creep lifetime, in association with important damage in the form of cavities or cracks (for example). The corresponding indentation creep compliance is relatively large, including at relatively low-temperature ( $T_{dwell} = 25^\circ\text{C}$  and  $T_{dwell} = 100^\circ\text{C}$ : see Fig. 7). This effect possibly relates to the peculiar temperature-dependence of pipe-diffusivity through the dislocation cores, which dramatically differs from bulk diffusivity controlling the conventional, macroscopic creep response (see Fig. 3 of Ref. 37).

In nano-indentation straining conditions, the dislocation-dislocation distance is incidentally comparable (or even smaller) to the ODS particle-particle separation. Direct dislocation/particle contact is, therefore, highly probable, especially inside the indent-induced plastic zone. Vacancies emitted at particle/matrix interfaces are easily trapped and subsequently transported away through pipe-diffusion, yielding fast dislocation self-climb and significant creep compliance levels.<sup>30</sup> Indentation creep results thus directly scale with the dose-dependent evolution of the vacancy flux intensity toward the local, indent-induced dislocation populations. The vacancy emission rate of ODS-3 particles is possibly affected by the dose-dependent evolutions of the particle/matrix interface topology and the core/shell particle structuration (see Sec. V A and Ref. 38).

### 2. Indentation creep response after irradiation at $T_{irr} = 500^\circ\text{C}$

The dose-dependent evolution of the indentation creep compliance is negligible, after irradiation at  $T_{irr} = 500^\circ\text{C}$  (see Fig. 7). The corresponding particle-size changes are likewise small, at least up to 25 dpa. The local vacancy flux can, therefore, not sustain a high creep/climb straining rate, up to  $T_{dwell} = 500^\circ\text{C}$ . ODS-3 thus resists creep-induced failure despite the presence of a high indent-induced dislocation density and important radiation damage accumulation. Interestingly, no significant positron lifetime increase is noted up to 525 nm depth (after irradiation at  $500^\circ\text{C}$ ), where the dose level reaches up to 35 dpa. Low post-irradiation creep compliance amplitude may, therefore, persist well beyond 25 dpa.

### 3. Indentation creep after irradiation at $T_{irr} = 600^\circ\text{C}$

The indentation creep compliance and positron lifetime are temperature-dependent and clearly distinct from the results obtained after  $T_{irr} = 500^\circ\text{C}$  (please refer to Fig. 7), in the 35–60 dpa dose range. The present  $T_{irr}$ -dependent changes are associated with significant particle size reduction and open volume growth, at the particle/matrix interfaces. These conditions contribute to (local) vacancy flux enhancement and, therefore, to significant creep-rate increase from  $T_{dwell} = 100^\circ\text{C}$  and upward (Fig. 7). The positron lifetime measured at 375–525 nm depth is in contrast mostly constant, indicating a weaker dose dependence of the indentation creep strain rate, beyond 40 dpa.

The post-irradiation indentation creep compliance of ODS-3 is in any case much smaller than in reference (ODS particle-free) Fe–Cr steels, under comparable irradiation and testing

conditions.<sup>62,63</sup> The present results thus highlight the beneficial effect of the ODS particles, during the late stages of the creep lifetime.

## VI. CONCLUSIONS

This paper is an experimental investigation of the micro-mechanical response of different, post-irradiated ODS alloys. High-dose irradiation experiments were performed using dual 5 MeV Ni and mitigated 1.5 MeV He beams at  $T_{irr} = 500, 600,$  and  $700\text{ }^{\circ}\text{C}$  up to 40 dpa and  $\sim 5 \times 10^{16}\text{ He cm}^{-2}$ . The irradiation-induced micro-structural evolutions are investigated by means of TEM, PAS, and PLEPS measurements combined. The corresponding micro-mechanical response changes are evaluated using nano-indentation testing at room and elevated temperature, with and without applied dwell time. The main conclusions from these investigations are as follows:

- (1) No TEM-resolved radiation-induced defect clusters (dislocation loops, voids, or other defects) were detected in Fe-0.3Y<sub>2</sub>O<sub>3</sub> (ODS-1), Fe-0.2Ti-0.3Y<sub>2</sub>O<sub>3</sub> (ODS-2), and Fe-14Cr-0.2Ti-0.3Y<sub>2</sub>O<sub>3</sub> (ODS-3) alloys for  $T_{irr} \geq 500\text{ }^{\circ}\text{C}$ . This finding highlights the active role of ODS particles on the defect recombination, during high-temperature ion irradiation.
- (2) Combination of HRTEM observations and PLEPS analysis shows that the chemical composition significantly affects the initial particle/matrix interface configuration. For instance, the addition of 0.2%Ti changes the particle/matrix interface from coherent in Fe-0.3Y<sub>2</sub>O<sub>3</sub> (ODS-1), to incoherent in Fe-0.2Ti-0.3Y<sub>2</sub>O<sub>3</sub> and Fe-14Cr-0.2Ti-0.3Y<sub>2</sub>O<sub>3</sub> alloys (ODS-2 and ODS-3 alloys, respectively).
- (3) The particle dose/temperature stability domain of Fe-14Cr-0.2Ti-0.3Y<sub>2</sub>O<sub>3</sub> (ODS-3) alloy is broader than the dose/temperature stability domain of Fe-0.2Ti-0.3Y<sub>2</sub>O<sub>3</sub> (ODS-2) and Fe-0.3Y<sub>2</sub>O<sub>3</sub> (ODS-1) alloys.
- (4) The proposed indentation analysis method is highly sensitive to the dose-dependent changes in the particle size distribution. In Fe-0.3Y<sub>2</sub>O<sub>3</sub> (ODS-1) alloy, for instance, the irradiation-induced dissolution of the fine particles yields a significant increase in the (micro) work-hardening rate. In Fe-0.2Ti-0.3Y<sub>2</sub>O<sub>3</sub> (ODS-2) and Fe-14Cr-0.2Ti-0.3Y<sub>2</sub>O<sub>3</sub> (ODS-3) alloys, in contrast, the stable post-irradiation particle size is associated with a stable (micro) work-hardening rate.
- (5) The indentation creep response is associated with a specific plasticity mechanism involving high dislocation densities and possibly self-climb due to point defect diffusion through the core region of the indent-induced dislocations. These conditions (high stress and high dislocation densities) are characteristic of the final stages of the creep lifetime. Hence, high-temperature indentation can be an effective screening test, for estimating the (late) creep response of ODS materials.
- (6) Fe-14Cr-0.2Ti-0.3Y<sub>2</sub>O<sub>3</sub> (ODS-3) alloy has been tested at elevated indentation temperatures up to  $600\text{ }^{\circ}\text{C}$ . The indentation creep compliance is mostly temperature and dose-independent, after irradiation at  $T_{irr} = 500\text{ }^{\circ}\text{C}$ . In contrast, the indentation creep compliance markedly decreases with temperature after irradiation at  $T_{irr} = 600\text{ }^{\circ}\text{C}$ . This evolution is concurrent with the irradiation-induced changes in the particle/matrix interface

topology, as evidenced by the positron annihilation PLEPS measurements (Detection of interfacial open volume variations.).

## ACKNOWLEDGMENTS

This work was performed under the aegis of Indo-French collaboration: *Agreement on basic research and modelling of physical phenomena*, as per the Implementing Agreement on Dislocation-precipitate interaction under high-temperature deformation in model ODS alloys. This work was partly funded by Grant No. VEGA 1/0477/16 and also contributes to the Joint Programme on Nuclear Materials (JPNM) of the European Energy Research Alliance (EERA).

## AUTHOR DECLARATIONS

### Conflicts of Interest

The authors have no conflicts to disclose.

### Author Contributions

**C. Robertson:** Conceptualization (lead); Data curation (lead); Formal analysis (equal); Funding acquisition (lead); Investigation (lead); Methodology (lead); Software (equal); Writing – original draft (lead); Writing – review & editing (lead). **M. H. Mathon:** Formal analysis (equal); Investigation (equal); Software (equal); Writing – original draft (equal). **B. K. Panigrahi:** Formal analysis (equal); Investigation (equal); Writing – original draft (equal). **S. Amirthapandian:** Formal analysis (equal); Investigation (equal). **S. Sojak:** Formal analysis (equal); Investigation (equal); Software (equal); Writing – original draft (equal). **S. Santra:** Formal analysis (equal); Investigation (equal); Writing – original draft (equal).

## DATA AVAILABILITY

The data that support the findings of this study are available within the article.

## REFERENCES

- <sup>1</sup>A. Ramar, P. Spätig, and R. Schäublin, *J. Nucl. Mater.* **382**, 210–216 (2008).
- <sup>2</sup>D. A. McClintock, M. A. Sokolov, D. T. Hoelzer, and R. K. Nanstad, *J. Nucl. Mater.* **392**, 353–359 (2009).
- <sup>3</sup>I.-S. Kim, J. D. Hunn, N. Hashimoto, D. L. Larson, P. J. Maziasz, K. Miyahara, and E. H. Lee, *J. Nucl. Mater.* **280**, 264–274 (2000).
- <sup>4</sup>P. Pareige, M. K. Miller, R. E. Stoller, D. T. Hoelzer, E. Cadel, and B. Radigue, *J. Nucl. Mater.* **360**, 136–142 (2007).
- <sup>5</sup>H. Kishimoto, K. Yutani, R. Kasada, and A. Kimura, *Fusion Eng. Des.* **81**, 1045–1049 (2006).
- <sup>6</sup>H. Kishimoto, R. Kasada, O. Hashitomi, and A. Kimura, *J. Nucl. Mater.* **386–388**, 533–536 (2009).
- <sup>7</sup>A. Ramar, N. Baluc, and R. Schäublin, *J. Nucl. Mater.* **367–370**, 217–221 (2007).
- <sup>8</sup>S. Yamashita, N. Akasaka, and S. Ohnuki, *J. Nucl. Mater.* **329–333**, 377–381 (2004).
- <sup>9</sup>M. K. Miller, K. F. Russel, and D. T. Hoelzer, *J. Nucl. Mater.* **351**, 261–268 (2006).

- <sup>10</sup>A. Steckmeyer, M. Praud, B. Fournier, J. Malaplate, J. Garnier, J. L. Béchade, I. Tourmié, A. Tancray, A. Bougault, and P. Bonnaillie, *J. Nucl. Mater.* **405**, 95–100 (2010).
- <sup>11</sup>L. Toualbi, C. Cayron, P. Olier, J. Malaplate, M. Praud, M.-H. Mathon, D. Bossu, E. Rouesne, A. Montani, R. Logé, and Y. de Carlan, *J. Nucl. Mater.* **428**, 47–53 (2012).
- <sup>12</sup>P. Dubuisson, Y. D. Carlan, V. Garat, and M. Blat, *J. Nucl. Mater.* **428**, 6–12 (2012).
- <sup>13</sup>M. Praud, F. Momprou, J. Malaplate, D. Caillard, J. Garnier, A. Steckmeyer, and B. Fournier, *J. Nucl. Mater.* **428**, 90–97 (2012).
- <sup>14</sup>B. Fournier, A. Steckmeyer, A.-L. Rouffie, J. Malaplate, J. Garnier, M. Ratti, P. Wident, L. Ziolk, I. Tourmié, V. Rabeau, J. M. Gentzittel, T. Kruml, and I. Kubena, *J. Nucl. Mater.* **430**, 142–149 (2012).
- <sup>15</sup>M.-L. Lescoat, I. Monnet, J. Ribis, P. Dubuisson, Y. De Carlan, J.-M. Costantini, and J. Malaplate, *J. Nucl. Mater.* **417**, 266–269 (2011).
- <sup>16</sup>J.-L. Béchade, D. Menu, M.-L. Lescoat, B. Sitaud, S. Schlutig, P. L. Solari, I. Llorens, H. Hermange, Y. De Carlan, J. Ribis, and L. Toualbi, *J. Nucl. Mater.* **428**, 183–191 (2012).
- <sup>17</sup>J. Ribis, M.-L. Lescoat, Y. de Carlan, J.-M. Costantini, I. Monnet, T. Cozzika, F. Delabrouille, and J. Malaplate, *J. Nucl. Mater.* **417**, 262–265 (2011).
- <sup>18</sup>M.-L. Lescoat, J. Ribis, A. Gentils, O. Kaïtasov, Y. De Carlan, and A. Legris, *J. Nucl. Mater.* **428**, 176–182 (2012).
- <sup>19</sup>S. Santra, S. Amirthapandian, S. Balaji, B. K. Panigrahi, Y. Serruys, and C. Robertson, *J. Nucl. Mater.* **528**, 151861 (2020).
- <sup>20</sup>C. Robertson, B. K. Panigrahi, S. Balaji, S. Kataria, Y. Serruys, M.-H. Mathon, and C. S. Sundar, *J. Nucl. Mater.* **426**, 240–246 (2012).
- <sup>21</sup>A. J. London, S. Santra, S. Amirthapandian, B. K. Panigrahi, R. M. Sarguna, S. Balaji, R. Vijay, C. S. Sundar, S. Lozano-Perez, and C. R. M. Grovenor, *Acta Mater.* **97**, 223–233 (2015).
- <sup>22</sup>O. Tissot, C. Pareige, E. Meslin, B. Décamps, and J. Henry, *Mater. Res. Lett.* **5**(2), 117–123 (2017).
- <sup>23</sup>J. F. Ziegler, *Nucl. Instrum. Methods Phys. Res., Sect. B* **219–220**, 1027–1036 (2004).
- <sup>24</sup>M. H. Mathon, Y. de Carlan, G. Geoffroy, X. Averty, A. Alamo, and C. H. de Novion, *J. Nucl. Mater.* **312**, 236–248 (2003).
- <sup>25</sup>C. Robertson, S. Poissonnet, and L. Boulanger, *J. Mater. Res.* **13**(8), 2123–2131 (1998).
- <sup>26</sup>R. Kasada, Y. Takayama, K. Yabuuchi, and A. Kimura, *Fusion Eng. Des.* **86**, 2658–2661 (2011).
- <sup>27</sup>S. Kataria, “Nano-mechanical characterization of thin films and surfaces,” Doctoral thesis (University of Madras, 2010).
- <sup>28</sup>W. D. Nix and H. J. Gao, “Indentation size effects in crystalline materials: A law for strain gradient plasticity,” *J. Mech. Phys. Solids* **46**, 411–425 (1998).
- <sup>29</sup>R. Kasada, S. Konishi, K. Yabuuchi, S. Nogami, M. Ando, D. Hamaguchi, and H. Tanigawa, *Fusion Eng. Des.* **89**, 1637–1641 (2014).
- <sup>30</sup>D. L. Krumwiede, T. Yamamoto, T. A. Saleh, S. A. Maloy, G. R. Odette, and P. Hosemann, *J. Nucl. Mater.* **504**, 135–143 (2018).
- <sup>31</sup>M. A. Mattucci, I. Cherubin, P. Changizian, T. Skippon, and M. R. Daymond, *Acta Mater.* **207**, 116702 (2021).
- <sup>32</sup>P. Haušild, *J. Nucl. Mater.* **551**, 152987 (2021).
- <sup>33</sup>P. Zhu, Y. Zhao, S. Agarwal, J. Henry, and S. J. Zinkle, *Mater. Des.* **213**, 110317 (2022).
- <sup>34</sup>C. Robertson and K. Gururaj, *J. Nucl. Mater.* **415**, 167–178 (2011).
- <sup>35</sup>M. Dao, N. Chollacoop, K. J. Van Vliet, T. A. Venkatesh, and S. Suresh, *Acta Mater.* **49**, 3899–3918 (2001).
- <sup>36</sup>J. L. Bucaille, S. Stauss, E. Felder, and J. Michler, *Acta Mater.* **51**, 1663–1678 (2003).
- <sup>37</sup>C. Robertson, S. Poissonnet, B. K. Panigrahi, and C. S. Sundar, *Procedia Eng.* **130**, 1105–1109 (2015).
- <sup>38</sup>T. D. Swinburne, K. Arakawa, H. Mori, H. Yasuda, M. Isshiki, K. Mimura, M. Uchikoshi, and S. L. Dudarev, *Sci. Rep.* **6**, 30596 (2016).
- <sup>39</sup>A. Vehanen, K. Saarinen, P. Hautojärvi, and H. Huomo, *Phys. Rev. B* **35**, 4606–4610 (1987).
- <sup>40</sup>C. Hügenschmidt *et al.*, *Appl. Surf. Sci.* **255**, 29–32 (2008).
- <sup>41</sup>P. Sperr, W. Egger, G. Kögel *et al.*, *Appl. Surf. Sci.* **255**, 35–38 (2008).
- <sup>42</sup>P. Kirkegaard and M. Eldrup, *Comput. Phys. Commun.* **3**, 240 (1972).
- <sup>43</sup>R. Rajaraman, G. Amarendra, and C. S. Sundar, *Phys. Status Solidi C* **6**(11), 2285–2290 (2009).
- <sup>44</sup>D. Brimbal, B. Decamps, A. Barbu, E. Meslin, and J. Henry, *J. Nucl. Mater.* **418**, 313–315 (2011).
- <sup>45</sup>Z. Yao, M. L. Jenkins, M. Hernandez-Mayoral, and M. A. Kirk, *Philos. Mag.* **90**, 4623–4634 (2010).
- <sup>46</sup>V. Kuksenko, “Model oriented irradiation experiments in Fe-Cr model alloys, materials science,” Doctoral Thesis (Université de Rouen, 2011).
- <sup>47</sup>H. Ohkubo, Z. Tang, Y. Nagai, M. Hasegawa, T. Tawara, and M. Kiritani, *Mater. Sci. Eng., A* **350**, 95 (2003).
- <sup>48</sup>L. C. Damonte, M. A. Taylor, J. Desimoni, and J. Runco, *Radiat. Phys. Chem.* **76**, 248 (2007).
- <sup>49</sup>V. Krsjak, J. Kuriplach, T. Shena, V. Sabelovac, K. Sato, and Y. Dai, *J. Nucl. Mater.* **456**, 382–388 (2015).
- <sup>50</sup>T. Troev, A. Markovski, S. Peneva, and T. Yoshiie, *J. Nucl. Mater.* **359**, 93–101 (2006).
- <sup>51</sup>D. Murali, B. K. Panigrahi, M. C. Valsakumar, S. Chandra, C. S. Sundar, and B. Raj, *J. Nucl. Mater.* **403**, 113–116 (2010).
- <sup>52</sup>D. Murali, B. K. Panigrahi, M. C. Valsakumar, and C. S. Sundar, *J. Nucl. Mater.* **419**, 208–212 (2011).
- <sup>53</sup>D. Mordehai and G. Martin, *Phys. Rev. B* **84**, 014115 (2011).
- <sup>54</sup>P. Olsson and C. Domain, *Phys. Rev. B* **75**, 014110 (2007).
- <sup>55</sup>T. R. Allen, J. Gan, J. I. Cole, M. K. Miller, J. T. Busby, S. Shuthanandan, and S. Thevuthasan, *J. Nucl. Mater.* **375**, 26–37 (2008).
- <sup>56</sup>J. Ribis, I. Mouton, C. Baumier, A. Gentils, M. Loyer-Prost, L. Lunéville, and D. Siméone, *Nanomaterials* **11**, 2590 (2021).
- <sup>57</sup>A. J. London, “Irradiation damage of oxide dispersion strengthened steels,” Ph.D. thesis (University of Oxford, 2016).
- <sup>58</sup>K. Gururaj, C. Robertson, and M. Fivel, *J. Nucl. Mater.* **459**, 194–204 (2015).
- <sup>59</sup>C. S. Shin, C. F. Robertson, and M. C. Fivel, *Philos. Mag.* **87**(24), 3657–3669 (2007).
- <sup>60</sup>E. Materna-Morris, R. Lindau, H.-C. Schneider, and A. Möslang, *Fusion Eng. Des.* **98–99**, 2038–2041 (2015).
- <sup>61</sup>C. F. Robertson and M. C. Fivel, *J. Mater. Res.* **14**(6), 2251–2258 (1999).
- <sup>62</sup>M. Arai, *J. Press. Vessel Technol.* **139**, 021403–021401 (2017).
- <sup>63</sup>P. Nogning Kamta, A. Mejias, F. Roudet, G. Louis, M. Touzin, and D. Chicot, *Mater. Sci. Eng., A* **652**, 315–324 (2016).